Letter

Heterostructural alloy phase diagram for $(Cd_{1-x}Zn_x)_3As_2$

Chase Brooks [1] and Stephan Lany [2]

[1]*Department of Physics, University of Colorado, Boulder, Colorado 80309, USA*
[2]*National Renewable Energy Laboratory, Golden, Colorado 80401, USA*

Alloying the topological semimetal Cd_3As_2 with Zn_3As_2 provides a potential route for controlling the electronic properties. We predict the alloy phase diagram from first-principles calculations, considering that both end members have a crystal structure derived from the antifluorite lattice, but with different arrangements of the unoccupied cation sites. To overcome the limitations of the regular solution approximation and to include short-range order effects, we perform Monte Carlo simulations, parameterize the temperature dependence of the mixing enthalpy ΔH_m, and perform thermodynamic integration of the free energy. The resulting phase diagram exhibits features that are unique to heterostructural alloy systems and provides computational predictions of solubility limits and composition ranges that are stable against spinodal decomposition.

Introduction. Alloys formed between compounds with different crystal structures, commonly known as heterostructural alloys, are a rapidly evolving means of advancement in solid-state material synthesis. This unique class of mixtures has many applications, including fine-tuning of material properties [1], fabricating metastable materials at compositions that are otherwise inaccessible [2], and creating negative-pressure polymorphs [3]. One of the most important aspects of studying heterostructural alloys is determining the composition dependence of the alloy mixing enthalpies in the different possible crystal structures. First-principles density functional theory (DFT) and cluster expansion methods have been very successful in modeling the formation of both isostructural and heterostructural alloys and sampling their configuration space [4–12]. In this work, we apply first-principles Monte Carlo sampling to study the combined effects of short-range order (SRO) and substitutions on several nonequivalent symmetry sites, and we utilize a thermodynamic integration to fully describe the temperature and composition dependence of alloy free energies.

Cd_3As_2 is a three-dimensional Dirac semimetal with sustained scientific interest. However, intrinsic point defects, recently found to be predominantly Cd interstitials [13], induce *n*-type doping and an elevated Fermi level after growth under typical synthesis conditions [13–17]. This unintentional self-doping effect inhibits access to the unique topological band structure features of Cd_3As_2. Conversely, Zn_3As_2 is a trivial semiconductor with a direct band gap of 1.0 eV and typically forms as *p*-type [18]. The alloy between these two compounds, $(Cd_{1-x}Zn_x)_3As_2$, is then expected to undergo both a crossover from *n*- to *p*-type and a topological phase transition from Dirac semimetal to semiconductor with increasing *x*. Both of these features were observed experimentally [19–21]. The purpose of the present work is to determine a detailed model for the phase behavior as a function of temperature and composition. Furthermore, the present results also provide representative atomic structure models for future electronic structure and doping studies.

The ground state of Cd_3As_2 is a body-centered tetragonal structure (space group 142, $I4_1/acd$) [22] with three distinct Wyckoff positions for both cations and anions. Zn_3As_2 was observed with this same structure [23] as well as a related primitive tetragonal structure (space group 137, $P4_2/nmc$) [24]. Both structures are obtained by constructing supercells of an antifluorite lattice with an ordered set of cation empty sites [22,25], and the only difference between the two is in the ordered stacking of these empty sites, i.e., they can be viewed as different polytypes. For our choice of DFT functional, namely, the strongly constrained and appropriately normed meta generalized gradient approximation (SCAN meta-GGA) [26], we find $P4_2/nmc$ to be the lower-energy structure for Zn_3As_2, so we consider it to be the ground state herein. The $(Cd_{1-x}Zn_x)_3As_2$ alloy was previously observed in this structure [23], but has also recently been seen to transition from body-centered to primitive tetragonal and then back to body-centered as *x* is increased [20].

With the backdrop of the currently somewhat inconclusive experimental picture, we here study this heterostructural alloy system by performing first-principles Metropolis Monte Carlo (MC) sampling in both crystal structures. We develop a model that captures temperature-dependent SRO effects in the enthalpy of mixing between the two compounds and then use this model to predict the alloy phase diagram with the crossover of the preferred crystal structure and with the solubility limits as functions of temperature and composition.

Methods. We obtained DFT total energies of alloy supercells with the projector augmented wave (PAW) method [27] as implemented in the VASP code [28]. While the MC energy sampling made use of a DFT based MC workflow [10] with a standard GGA functional [29], calculations of the final configuration energies used the SCAN functional with spin-orbit coupling, which is known to give improved energy differences between atomic configurations [30] and has been found to more accurately describe Cd_3As_2 [13]. Additional details on DFT calculations are given in the Supplemental Material [31].
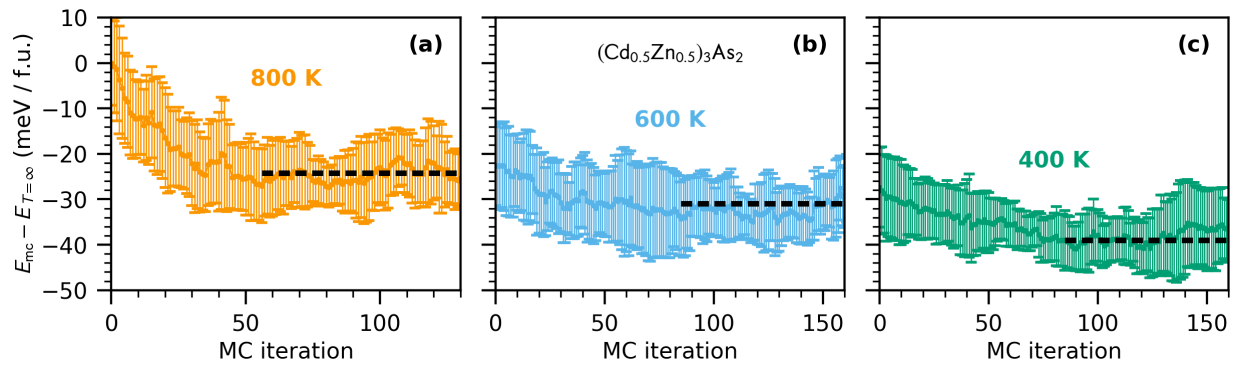
FIG. 1. Monte Carlo simulated annealing of $(Cd_{0.5}Zn_{0.5})_3As_2$ for the Cd_3As_2 ground-state crystal structure, averaged over ten independent samples and equilibrated sequentially at (a) 800, (b) 600, and (c) 400 K. Energies are measured with respect to the average of the initial random ($T = \infty$) configurations. Error bars indicate the standard deviation across the independent MC runs at each iteration.

Common tangent construction between free energy plots was performed using the optimize package in SCIPY [32].

First-principles Monte Carlo. In preliminary calculations we found that the Zn substitution energies vary markedly among the three nonequivalent Cd sites of the Cd_3As_2 ground-state structure. Additionally, we observed significant changes in alloy total energies when varying cation configurations for both the Cd_3As_2 and Zn_3As_2 structures, indicating considerable SRO effects. Both of these contributions give rise to nonrandom distributions of cations within the alloy. Therefore, instead of modeling a random alloy—e.g., with special quasirandom structures—we performed MC simulations which are capable of capturing the temperature-dependent effects of SRO and yielding more realistic alloy configurations. While SRO is expected to be less pronounced for the isovalent substitutions we consider here, compared to, e.g., the exceedingly strong effects in heterovalent alloys [33], we find it is strong enough that it should be taken into account.

As initial configurations for the MC simulations, we constructed 80-atom supercells for both the $I4_1/acd$ and $P4_2/nmc$ structures over the full $(Cd_{1-x}Zn_x)_3As_2$ alloy composition range in steps of $\Delta x = 0.125$. Here, the lattice constants are approximated by Vegard's Law, and the cation configurations are sampled by ten explicitly random Cd/Zn occupations for each composition, corresponding to an initial $T = \infty$ infinite temperature limit. For each of the initial configurations, we performed independent MC equilibrations in the canonical NVT ensemble. Specifically, the cation distribution is sampled by mutual swapping of randomly chosen Cd and Zn sites, while using the resulting DFT energy after atomic-force relaxation to accept or reject the trial configuration in accordance with the Boltzmann probability distribution.

To obtain configurations associated with temperatures in the range of interest, we performed simulated annealing [34] by sequentially equilibrating the MC simulations at 800, 600, and 400 K, i.e., corresponding to Cd_3As_2 growth temperatures accessible by thin film and bulk synthesis as in previous work [13]. Averaging over ten independent runs for each composition allows for the determination of an effective ensemble average of the energy E_x of the alloy at a given temperature, noting that the energy E is virtually identical to the enthalpy H at ambient pressure in the solid state. The present model

maintains the sublattice of unoccupied sites of the antifluorite lattice in either polytype. Disorder in the distribution of the empty sites is, in principle, also possible, presumably being responsible for the cubic phase transition at 900 to 1000 K [35], but it is expected to be of minor importance in the lower temperature range of interest here.

The resulting average energies for the simulated annealing of $(Cd_{0.5}Zn_{0.5})_3As_2$ with the Cd_3As_2 crystal structure are shown in Fig. 1. Energies are measured with respect to the average of the initial random configurations. Short-range order at finite temperature gives rise to a significant decrease in energy from the fully randomized starting configuration, i.e., around 40 meV per formula unit (f.u.) at 400 K. Furthermore, the systematic energy changes between finite temperatures suggest a smooth variation as a function of temperature. Because SRO clearly has a significant impact on the average energy of the alloys, it is therefore essential that a model of the alloy mixing enthalpy account for this temperature dependence.

Thermodynamic free energy integration. A common starting point for describing alloy thermodynamics is the regular solution model, where the configurational entropy of mixing is assumed to be equal to the limit of ideal random site occupations, and the mixing enthalpy is considered to be independent of the temperature [36,37]. The ideal random alloy configurational entropy is given by

$$\Delta S_m(T = \infty) = -k_B[x\ln(x) + (1-x)\ln(1-x)], \quad (1)$$

where x and $(1-x)$ are the fractional compositions of the competing atomic species. The enthalpy of mixing is typically modeled as a quadratic function of the alloy composition with a constant bowing parameter, i.e., $\Delta H_m = \Omega x(1-x)$ [37]. We define here a model that incorporates a temperature dependence of the mixing enthalpy through the interaction parameter $\Omega(T)$. Specifically, with the relative polytype energies E_0 and E_1 of the end compounds included, the mixing enthalpy is given by

$$\Delta H_m(T) = \Omega(T) \cdot x(1-x) + (1-x)E_0 + xE_1. \quad (2)$$

For each of the two polytypes, we fit bowing parameters $\Omega(T)$ to the mixing enthalpies of the initial random configurations as well as those resulting from the MC equilibrations
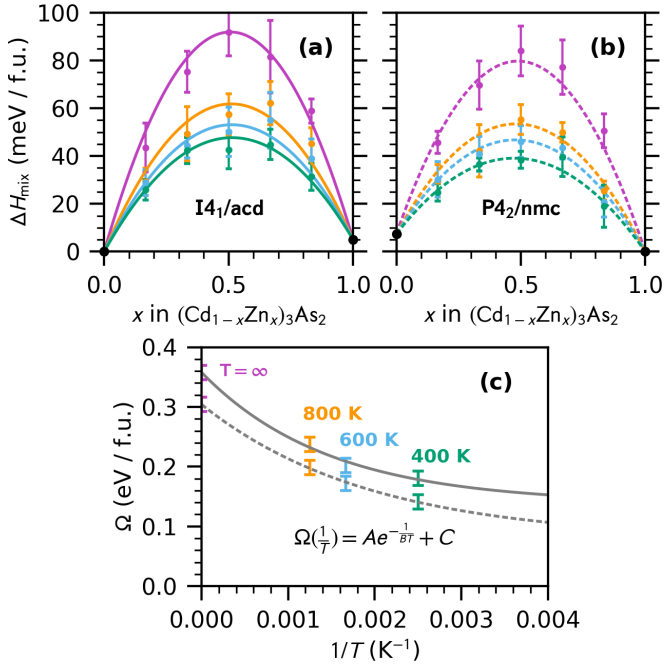
FIG. 2. Temperature dependent alloy mixing enthalpy ΔH_m data and quadratic fits for Monte Carlo simulations of (a) space group $I4_1/acd$ (solid) and (b) space group $P4_2/nmc$ (dashed) as functions of composition x. Energies are measured with respect to the respective ground states at the end-point compositions ($x = 0$ and $x = 1$). (c) Discrete MC data and exponential decay function fit for the quadratic bowing parameter Ω of both structures as a function of reciprocal temperature.

at the different temperatures. Figure 2 shows the raw mixing enthalpy data and the quadratic fits to Eq. (2) as a function of composition. Data are shown for infinite temperature (random seed) as well as 800, 600, and 400 K. We tested the possibility of an asymmetric shape of ΔH_m by fitting third-order polynomials, but found insufficient statistical significance. Comparing Figs. 2(a) and 2(b), we observe similar SRO effects in both structures. The magnitude of Ω at each temperature is large compared to the energy differences between the two polytypes at the endpoints: $E_1 = 5.0$ meV/f.u. for $I4_1/acd$ and $E_0 = 7.3$ meV/f.u. for $P4_2/nmc$. This comparably small energy difference between the two structures for both compounds is attributed to the two structures only being differentiated by the stacking of cation empty sites as discussed above.

Construction of a heterostructural alloy phase diagram requires a model for the free energy of mixing at all temperatures (see below). To this end, we first determine the T dependence of the mixing enthalpy by extrapolating the discrete set of bowing parameters from the MC simulations. Specifically, we model the temperature dependence of Ω with an exponentially decaying function in $1/T$, i.e.,

$$\Omega\left(\frac{1}{T}\right) = A e^{-\frac{1}{BT}} + C, \qquad (3)$$

where A, B, and C are empirical fit parameters. This functional form for Ω captures an initial value $A + C$ at $T = \infty$ corresponding to the regular solution limit, and then decreases

with lower temperatures to a limiting value C as $T \to 0$. The difference $A - C$ captures the maximal energy lowering afforded by SRO while maintaining a long-range disordered state. Figure 2(c) shows numerical fits to this exponential decay function for Ω as a function of $1/T$. Substituting this functional form for Ω into Eq. (2) yields a temperature-dependent mixing enthalpy that is used for further analysis in the following.

At finite temperatures in a MC simulation—where configurational entropy is not explicitly known—the free energy of mixing $\Delta G_m = \Delta H_m - T\Delta S_m$ is typically obtained via thermodynamic integration starting from either zero or infinite temperature [38,39]. Either case makes use of a starting point where configurational entropy is known exactly, either $\Delta S_m = 0$ for $T = 0$ or ΔS_m given by Eq. (1) for $T = \infty$. We employ the infinite temperature starting point because it coincides with the initial random configurations for the simulated annealing. In this framework, the free energy of mixing at finite temperature is given by

$$\Delta G_m(T) = T\left[-\Delta S_m(\infty) + \int_0^{\frac{1}{T}} \Delta H_m\left(\frac{1}{T'}\right) d\left(\frac{1}{T'}\right) \right], \quad (4)$$

where the mixing enthalpy $\Delta H_m(1/T)$ is given by substituting Eq. (3) into Eq. (2). The chosen analytic expression for $\Omega(1/T)$ above makes it possible to evaluate the integral in Eq. (4) and obtain the free energies for any composition and temperature not explicitly sampled with MC. Furthermore, the finite-temperature configurational entropy can then be determined by $\Delta S_m = (\Delta H_m - \Delta G_m)/T$ if needed.

Phase diagram. The Gibbs free energy of mixing ΔG_m describes the free energy of the alloy relative to the pure end compounds, thereby eliminating any dependence on chemical potentials and associated partial pressures in the gas phase. Further, we did not attempt to evaluate vibrational contributions which are expected to cancel to a large extent, due to the chemical and structural similarity of the end compounds. Thus, having determined $\Delta G_m(x, T)$ via Eq. (4) for both polytypes, we can construct a phase diagram containing the composition limits for binodal and spinodal decomposition.

The binodal line defines the global free energy minimum for phase coexistence, thereby describing the thermodynamic solubility limit, and is obtained via common tangent construction. The spinodal line further describes metastable regions that resist small fluctuations in composition, and is determined by the condition $d^2\Delta G_m/dx^2 = 0$. Phase diagram construction for this temperature-dependent bowing parameter model follows a similar procedure to the conventional regular solution model [2,36]. For temperatures within the range of interest, we determine the binodal x points from common tangent construction, considering that the tangents can be either between or within the polytypes. The spinodal x points are determined for each polytype separately as the inflection points of the free energy curve. Repeating the process for each temperature gives a set of (x, T) points that collectively map out the alloy phase diagram.

For the phase diagram construction from the free energy expression, we utilized the SCIPY optimize package. The derivative of the free energy $\Delta G'_m(x) = d\Delta G_m/dx$ was evaluated numerically with second-order central differences and

then fit with a cubic spline interpolation. For the common tangent construction, we used the minimize function to find the values x_1 and x_2 with the smallest absolute difference between the derivatives of the two structures. However, the unique solution that corresponds to a common tangent has the additional constraint that—in addition to the derivatives being equal—the derivatives at those points must equal the slope of the line that connects them, i.e., $\Delta G'_{m,1}(x_1) = \Delta G'_{m,2}(x_2) = [\Delta G_{m,2}(x_2) - \Delta G_{m,1}(x_1)]/(x_2 - x_1)$. Imposing this constraint when minimizing the absolute difference between the derivatives gives the common tangent at a given temperature such that the solution points x_1 and x_2 then lie on the binodal lines. The spinodal lines were found by solving for the points at which the numerical derivative changes sign.

Previous work on phase diagrams of heterostructural alloys has highlighted the possibility of novel features beyond the regular solution model of isostructural alloys [2], including the decoupling of binodal and spinodal lines, resulting in access to much wider metastable (x, T) ranges where the alloys are stable against spinodal decomposition. The detailed features of heterostructural phase diagrams depend on whether the relation between the crystal structures is displacive or reconstructive, and on the relative magnitude of the end point polymorph energies and the interaction parameters. As discussed in detail in Ref. [2], in the case of a displacive relationship, only the lower-energy structure type of the respective end compounds is dynamically stable, which leads to a single, but possibly strongly nonparabolic mixing enthalpy. In contrast, a reconstructive relationship involves energy barriers in the structure transition, stabilizing the higher-energy polymorph or polytype. In this case, we obtain two distinct free energy curves over the entire composition range.

Figure 3(a) shows the temperature-composition phase diagram for $(Cd_{1-x}Zn_x)_3As_2$, calculated from the above-defined free energy model. The relationship between the two polytypes is reconstructive because the conversion requires overcoming energy barriers associated with the reordering of the unoccupied cation sites. For the two temperatures of 300 K and 370 K, Figs. 3(b) and 3(c) show the two free energy curves with the corresponding common tangent construction. (Similar figures for 400 and 500 K are shown in the Supplemental Material [31].) The structural transition just below $x = 0.2$ is sharp due to the reconstructive transformation, and weakly temperature dependent. It occurs at Cd-rich compositions, which is a consequence of the fact that interaction parameters $\Omega(T)$ are smaller in the $P4_2/nmc$ (Zn_3As_2) than in the $I4_1/acd$ (Cd_3As_2) structure, even though the relative magnitude of the end point energies E_0 and E_1 would favor a transition in the Zn-rich regime (cf. Fig. 2). The structure transition occurs at higher yet comparable Zn compositions than observed in Ref. [20], but the reported change back to $I4_1/acd$ in the Zn-rich regime does not follow from the present model.

The (binodal) miscibility gap narrows quickly around 400 K, but persists up to high temperatures around the critical composition for structure transition (near $x = 0.2$), forming a characteristic "chimney" structure in the phase diagram [Fig. 3(a)]. For temperatures around 370 K, we observe two common tangents [cf. Fig. 3(c)], one between the two struc-
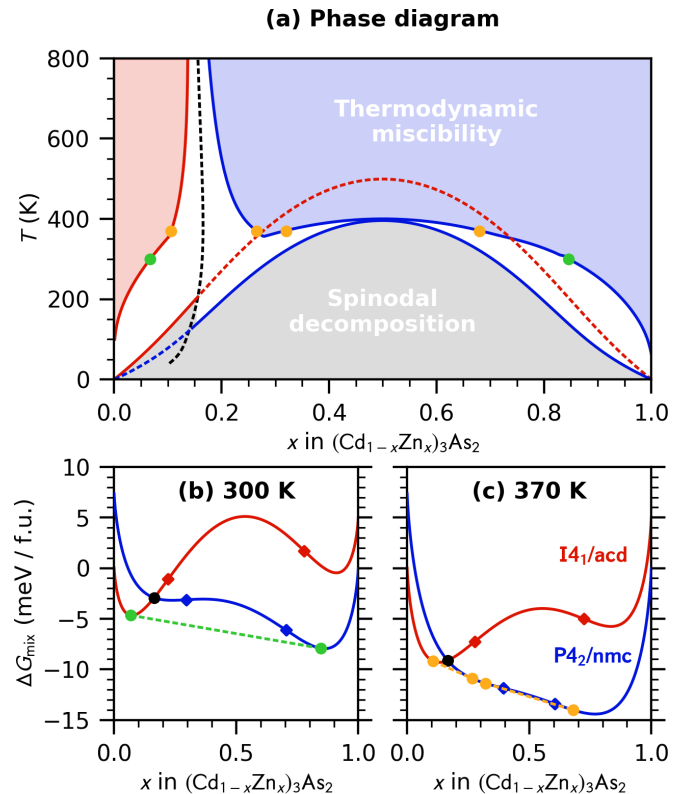
FIG. 3. (a) Temperature-composition phase diagram for the $(Cd_{1-x}Zn_x)_3As_2$ heterostructural alloy. The miscibility regions for the two structures are colored red and blue, and the metastable region between them is colored white. Corresponding free energies of mixing ΔG_m at (b) $T = 300$ K and (c) $T = 370$ K are shown as a function of composition x. The black dashed line in (a) marks the minimum free energy crossover between the two structures, illustrated by black dots in (b) and (c). Green and orange dots represent points on the binodal lines as governed by common tangent construction. Diamonds indicate inflection points that determine the spinodal lines in (a), shown as solid (dashed) for compositions at which the respective structure is stable (metastable).

tures and one within the $P4_2/nmc$ (Zn_3As_2) structure. The possibility of a coexistence of two common tangents is also a unique feature of heterostructural alloys. It was not observed in Ref. [2] because the phase diagrams in that work were dominated by the contribution of the polymorph energies in contrast to the stronger effect of the interaction parameter in the present case.

In contrast to the binodal lines, the spinodal lines are determined for each structure separately. In the regular solution model, the spinodal lines are exact parabolas, but in our present model they deviate from parabolic, particularly near the endpoints. This deviation is a result of the decreasing magnitude of $\Omega(T)$ with temperature, resulting in a wider range of metastable compositions at low temperatures. Overall, the predicted phase diagram in Fig. 3 suggests thermodynamic miscibility for most compositions above about 400 K, which corresponds to the lower limit of common synthesis conditions [14,40]. The narrow binodal miscibility gap around the structural transition can likely be overcome by thin-film synthesis, e.g., via molecular beam epitaxy [14,40,41], where

the interatomic mixing can result from the deposition process and does not need to be driven by thermodynamics. Above room temperature, the $(Cd_{1-x}Zn_x)_3As_2$ alloy is predicted to be metastable against spinodal decomposition up to Zn compositions around $x = 0.3$.

The $(Cd_{1-x}Zn_x)_3As_2$ structures generated by the present MC simulations (available in the Supplemental Materials) will serve for future investigations, extending upon our previous study in pure Cd_3As_2 [13], where we used a combination of quasi-particle self-consistent *GW* electronic structure theory [42] and DFT calculations of defect formation energies. Interesting questions include how the Cd/Zn composition and the degree of short-range order affect the topological band structure and how defect-dopant interactions and alloy disorder alter the doping properties [43].

Conclusion. We constructed a heterostructural alloy phase diagram for $(Cd_{1-x}Zn_x)_3As_2$ based on first-principles total energy calculations. Monte Carlo simulated annealing revealed significant short-range order effects, reducing the mixing enthalpy ΔH_m by about a factor of $1/2$ compared to the random alloy in the temperature range of interest. The phase diagram reveals characteristic features for alloys with a structural phase transition between the end members, such as the coexistence of two miscibility gaps at a given temperature, and the persistence of a narrow miscibility gap around the structure transition up to high temperatures. The results suggest favorable mixing behavior of $(Cd_{1-x}Zn_x)_3As_2$ alloys, especially in thin film deposition, with stability against spinodal decomposition up to $x = 0.3$.

[1] A. Schleife, M. Eisenacher, C. Rödl, F. Fuchs, J. Furthmüller, and F. Bechstedt, *Ab initio* description of heterostructural alloys: Thermodynamic and structural properties of $Mg_xZn_{1-x}O$ and $Cd_xZn_{1-x}O$, Phys. Rev. B **81**, 245210 (2010).

[2] A. M. Holder, S. Siol, P. F. Ndione, H. Peng, A. M. Deml, B. E. Matthews, L. T. Schelhas, M. F. Toney, R. G. Gordon, W. Tumas, J. D. Perkins, D. S. Ginley, B. P. Gorman, J. Tate, A. Zakutayev, and S. Lany, Novel phase diagram behavior and materials design in heterostructural semiconductor alloys, Sci. Adv. **3**, e1700270 (2017).

[3] S. Siol, A. Holder, J. Steffes, L. T. Schelhas, K. H. Stone, L. Garten, J. D. Perkins, P. A. Parilla, M. F. Toney, B. D. Huey, W. Tumas, S. Lany, and A. Zakutayev, Negative-pressure polymorphs made by heterostructural alloying, Sci. Adv. **4**, eaaq1442 (2018).

[4] L. K. Teles, J. Furthmüller, L. M. R. Scolfaro, J. R. Leite, and F. Bechstedt, First-principles calculations of the thermodynamic and structural properties of strained $In_xGa_{1-x}N$ and $Al_xGa_{1-x}N$ alloys, Phys. Rev. B **62**, 2475 (2000).

[5] J. Z. Liu, G. Trimarchi, and A. Zunger, Strain-minimizing tetrahedral networks of semiconductor alloys, Phys. Rev. Lett. **99**, 145501 (2007).

[6] M. Muzyk, D. Nguyen-Manh, K. J. Kurzydłowski, N. L. Baluc, and S. L. Dudarev, Phase stability, point defects, and elastic properties of W-V and W-Ta alloys, Phys. Rev. B **84**, 104115 (2011).

[7] E. Antillon and M. Ghazisaeidi, Efficient determination of solid-state phase equilibrium with the multicell Monte Carlo method, Phys. Rev. E **101**, 063306 (2020).

[8] A. Seko, K. Shitara, and I. Tanaka, Efficient determination of alloy ground-state structures, Phys. Rev. B **90**, 174104 (2014).

[9] S. R. Bauers, A. Holder, W. Sun, C. L. Melamed, R. Woods-Robinson, J. Mangum, J. Perkins, W. Tumas, B. Gorman, A. Tamboli *et al.*, Ternary nitride semiconductors in the rocksalt crystal structure, Proc. Natl. Acad. Sci. USA **116**, 14829 (2019).

[10] A. Sharan and S. Lany, Computational discovery of stable and metastable ternary oxynitrides, J. Chem. Phys. **154**, 234706 (2021).

[11] R. W. Smaha, K. Yazawa, A. G. Norman, J. S. Mangum, H. Guthrey, G. L. Brennecka, A. Zakutayev, S. R. Bauers, P. Gorai, and N. M. Haegel, Synthesis and calculations of wurtzite $Al_{1-x}Gd_xN$ heterostructural alloys, Chem. Mater. **34**, 10639 (2022).

[12] C. L. Rom, R. W. Smaha, C. L. Melamed, R. R. Schnepf, K. N. Heinselman, J. S. Mangum, S.-J. Lee, S. Lany, L. T. Schelhas, A. L. Greenaway *et al.*, Combinatorial synthesis of cation-disordered manganese tin nitride $MnSnN_2$ thin films with magnetic and semiconducting properties, Chem. Mater. **35**, 2936 (2023).

[13] C. Brooks, M. van Schilfgaarde, D. Pashov, J. N. Nelson, K. Alberi, D. S. Dessau, and S. Lany, Band energy dependence of defect formation in the topological semimetal Cd_3As_2, Phys. Rev. B **107**, 224110 (2023).

[14] J. N. Nelson, I. A. Leahy, A. D. Rice, C. Brooks, G. Teeter, M. van Schilfgaarde, S. Lany, B. Fluegel, M. Lee, and K. Alberi, Direct link between disorder and magnetoresistance in topological semimetals, Phys. Rev. B **107**, L220206 (2023).

[15] R. Sankar, M. Neupane, S.-Y. Xu, C. J. Butler, I. Zeljkovic, I. Panneer Muthuselvam, F.-T. Huang, S.-T. Guo, S. K. Karna, M.-W. Chu *et al.*, Large single crystal growth, transport property and spectroscopic characterizations of three-dimensional Dirac semimetal Cd_3As_2, Sci. Rep. **5**, 12966 (2015).

[16] G. S. Jenkins, C. Lane, B. Barbiellini, A. B. Sushkov, R. L. Carey, F. Liu, J. W. Krizan, S. K. Kushwaha, Q. Gibson, T.-R. Chang, H.-T. Jeng, H. Lin, R. J. Cava, A. Bansil, and H. D.

Drew, Three-dimensional Dirac cone carrier dynamics in Na_3Bi and Cd_3As_2, Phys. Rev. B **94**, 085121 (2016).

[17] H. T. Chorsi, S. Yue, P. P. Iyer, M. Goyal, T. Schumann, S. Stemmer, B. Liao, and J. A. Schuller, Widely tunable optical and thermal properties of Dirac semimetal Cd_3As_2, Adv. Opt. Mater. **8**, 1901192 (2020).

[18] W. J. Turner, A. S. Fischler, and W. E. Reese, Physical properties of several II-V semiconductors, Phys. Rev. **121**, 759 (1961).

[19] L. M. Rogers, R. M. Jenkins, and A. J. Crocker, Transport and optical properties of the $Cd_{3-x}Zn_xAs_2$ alloy system, J. Phys. D **4**, 793 (1971).

[20] H. Lu, X. Zhang, Y. Bian, and S. Jia, Topological phase transition in single crystals of $(Cd_{1-x}Zn_x)_3As_2$, Sci. Rep. **7**, 3148 (2017).

[21] S. Nishihaya, M. Uchida, Y. Nakazawa, M. Kriener, Y. Kozuka, Y. Taguchi, and M. Kawasaki, Gate-tuned quantum Hall states in Dirac semimetal $(Cd_{1-x}Zn_x)_3As_2$, Sci. Adv. **4**, eaar5668 (2018).

[22] M. N. Ali, Q. Gibson, S. Jeon, B. B. Zhou, A. Yazdani, and R. J. Cava, The crystal and electronic structures of Cd_3As_2, the three-dimensional electronic analogue of graphene, Inorg. Chem. **53**, 4062 (2014).

[23] W. Zdanowicz, K. Lukaszewicz, and W. Trzebiatowski, Crystal structure of semiconducting system Cd_3As_2-Zn_3As_2, Bull. Acad. Pol. Sci. Ser. Chim **12**, 169 (1964).

[24] W. Zdanowicz, F. Krolicki, and P. Plenkiewicz, Preparation and semiconducting properties of pseudobinary solid solutions Zn_3As_2-Zn_3P_2, Acta Physica Polonica A **44**, 447 (1973).

[25] A. M. Conte, O. Pulci, and F. Bechstedt, Electronic and optical properties of topological semimetal Cd_3As_2, Sci. Rep. **7**, 45500 (2017).

[26] J. Sun, A. Ruzsinszky, and J. P. Perdew, Strongly constrained and appropriately normed semilocal density functional, Phys. Rev. Lett. **115**, 036402 (2015).

[27] P. E. Blöchl, Projector augmented-wave method, Phys. Rev. B **50**, 17953 (1994).

[28] G. Kresse and D. Joubert, From ultrasoft pseudopotentials to the projector augmented-wave method, Phys. Rev. B **59**, 1758 (1999).

[29] J. P. Perdew, K. Burke, and M. Ernzerhof, Generalized gradient approximation made simple, Phys. Rev. Lett. **77**, 3865 (1996).

[30] J. H. Yang, D. A. Kitchaev, and G. Ceder, Rationalizing accurate structure prediction in the meta-GGA SCAN functional, Phys. Rev. B **100**, 035132 (2019).

[31] See Supplemental Material at http://link.aps.org/supplemental/10.1103/PhysRevMaterials.8.L061201 for further computational details and additional plots of the free energies of mixing at higher temperatures. The compressed archive file contains crystal structure files of the alloy at different compositions after Monte Carlo simulated annealing.

[32] P. Virtanen, R. Gommers, T. E. Oliphant, M. Haberland, T. Reddy, D. Cournapeau, E. Burovski, P. Peterson, W. Weckesser, J. Bright, S. J. van der Walt, M. Brett, J. Wilson, K. J. Millman, N. Mayorov, A. R. J. Nelson, E. Jones, R. Kern, E. Larson, C. J. Carey, İ. Polat, Y. Feng, E. W. Moore, J. VanderPlas, D. Laxalde, J. Perktold, R. Cimrman, I. Henriksen, E. A. Quintero, C. R. Harris, A. M. Archibald, A. H. Ribeiro, F. Pedregosa, P. van Mulbregt, and SciPy 1.0 Contributors, SciPy 1.0: Fundamental algorithms for scientific computing in Python, Nat. Meth. **17**, 261 (2020).

[33] J. Pan, J. J. Cordell, G. J. Tucker, A. Zakutayev, A. C. Tamboli, and S. Lany, Perfect short-range ordered alloy with line-compound-like properties in the $ZnSnN_2$: ZnO system, npj Comput. Mater. **6**, 63 (2020).

[34] S. Kirkpatrick, C. D. Gelatt, Jr., and M. P. Vecchi, Optimization by simulated annealing, Science **220**, 671 (1983).

[35] A. Pietraszko and K. Łukaszewicz, Thermal expansion and phase transitions of Cd_3As_2 and Zn_3As_2, Phys. Stat. Sol. (a) **18**, 723 (1973).

[36] I. Ho and G. B. Stringfellow, Solid phase immiscibility in GaInN, Appl. Phys. Lett. **69**, 2701 (1996).

[37] G. B. Stringfellow, *Organometallic Vapor-Phase Epitaxy: Theory and Practice* (Elsevier, Amsterdam, 1999).

[38] K. Binder, Monte Carlo study of entropy for face-centered cubic Ising antiferromagnets, Z. Phys. B **45**, 61 (1981).

[39] J. J. Cordell, J. Pan, A. C. Tamboli, G. J. Tucker, and S. Lany, Probing configurational disorder in $ZnGeN_2$ using cluster-based Monte Carlo, Phys. Rev. Mater. **5**, 024604 (2021).

[40] A. D. Rice, K. Park, E. T. Hughes, K. Mukherjee, and K. Alberi, Defects in Cd_3As_2 epilayers via molecular beam epitaxy and strategies for reducing them, Phys. Rev. Mater. **3**, 121201(R) (2019).

[41] T. Schumann, M. Goyal, H. Kim, and S. Stemmer, Molecular beam epitaxy of Cd_3As_2 on a III-V substrate, APL Mater. **4**, 126110 (2016).

[42] D. Pashov, S. Acharya, W. R. Lambrecht, J. Jackson, K. D. Belashchenko, A. Chantis, F. Jamet, and M. van Schilfgaarde, Questaal: A package of electronic structure methods based on the linear muffin-tin orbital technique, Comput. Phys. Commun. **249**, 107065 (2020).

[43] A. Goyal, M. D. Sanders, R. P. O'Hayre, and S. Lany, Predicting thermochemical equilibria with interacting defects: $Sr_{1-x}Ce_xMnO_{3-\delta}$ alloys for water splitting, PRX Energy **3**, 013008 (2024).